Received: 5 April 2022 | Revised: 19 December 2022 | Accepted: 5 January 2023

DOI: 10.1002/wics.1606

FOCUS ARTICLE

WIREs COMPUTATIONAL STATISTICS

WILEY

Neuroimaging statistical approaches for determining neural correlates of Alzheimer's disease via positron emission tomography imaging

Daniel F. Drake[1] | **Gordana Derado**[2] | **Lijun Zhang**[3] | **F. DuBois Bowman**[1] | **for the Alzheimer's Disease Neuroimaging Initiative**

[1]Department of Biostatistics, School of Public Health, University of Michigan, Ann Arbor, Michigan, USA

[2]Department of Biostatistics and Bioinformatics, Rollins School of Public Health, Emory University, Atlanta, Georgia, USA

[3]Department of Population and Quantitative Health Science, Case Western Reserve University, Cleveland, Ohio, USA

Correspondence
Daniel F. Drake, Department of Biostatistics, School of Public Health, University of Michigan, Ann Arbor, MI, USA.
Email: dfdrake@umich.edu

Funding information
National Institute of Neurological Disorders and Stroke, Grant/Award Number: P50NS123067; Alzheimer's Disease Neuroimaging Initiative; National Institutes of Health, Grant/Award Number: U01 AG024904; National Institute on Aging

Edited by: Kimberly Sellers, Commissioning Editor and David Scott, Review Editor and Co-Editor-in-Chief

Abstract

Alzheimer's disease (AD) is a degenerative disorder involving significant memory loss and other cognitive deficits, manifesting as a progression from normal cognitive functioning to mild cognitive impairment to AD. The sooner an accurate diagnosis of probable AD is made, the easier it is to manage symptoms and plan for future therapy. Functional neuroimaging stands to be a useful tool in achieving early diagnosis. Among the many neuroimaging modalities, positron emission tomography (PET) provides direct regional assessment of, among others, brain metabolism, cerebral blood flow, amyloid deposition—all quantities of interest in the characterization of AD. However, there are analytic challenges in identifying early indicators of AD from these high-dimensional imaging data sets, and it is unclear whether early indicators of AD are more likely to emerge in localized patterns of brain activity or in patterns of correlation between distinct brain regions. Early PET-based analyses of AD focused on alterations in *metabolic activity* at the voxel-level or in anatomically defined regions of interest. Other approaches, including seed-voxel and multivariate techniques, seek to characterize *metabolic connectivity* by identifying other regions in the brain with similar patterns of activity across subjects. We briefly review various neuroimaging statistical approaches applied to determine changes in metabolic activity or metabolic connectivity associated with AD. We then present an approach that provides a unified statistical framework for addressing both metabolic activity and connectivity. Specifically, we apply a Bayesian spatial hierarchical framework to longitudinal metabolic PET scans from the Alzheimer's Disease Neuroimaging Initiative.

Data used in preparation of this article were obtained from the Alzheimer's Disease Neuroimaging Initiative (ADNI) database (https://adni.loni.usc.edu/). As such, the investigators within the ADNI contributed to the design and implementation of ADNI and/or provided data but did not participate in analysis or writing of this report. A complete listing of ADNI investigators can be found at: http://adni.loni.usc.edu/wp-content/uploads/how_to_apply/ADNI_Acknowledgement_List.pdf

https://doi.org/10.1002/wics.1606

This article is categorized under:
Statistical and Graphical Methods of Data Analysis > Analysis of High Dimensional Data
Statistical Learning and Exploratory Methods of the Data Sciences > Modeling Methods
Statistical Models > Bayesian Models

KEYWORDS

brain activation analysis, Alzheimer's disease, Bayesian modeling and inference, brain connectivity analysis, PET neuroimaging

1 | INTRODUCTION

Positron emission tomography (PET) neuroimaging has proven to be an extremely useful diagnostic tool in quantifying brain function. Depending on the ligand, PET scans can highlight specific function of the brain. One of the most important ligands, [^{18}F]-2-fluoro-2-deoxy-2-glucose (FDG), targets metabolic rates of glucose uptake, an indicator of neuronal activity. Studies have shown that alterations in cerebral metabolic activity can precede the clinical manifestation of dementia symptoms (Brown et al., 2014), particularly in Alzheimer's disease (AD) (Marcus et al., 2014). Other ligands, like [^{11}C]-Pittsburg Compound B (PiB) that measures amyloid deposits or [^{15}O]-H_2O that measures cerebral blood flow, also play a role in AD research.

AD is a progressive, degenerative disorder that attacks the brain's neurons, resulting in loss of memory, thinking and language skills, and behavioral changes; and is the most common cause of dementia, or loss of intellectual function, among people aged 65 and older. Clinicians can now diagnose AD with up to 90% accuracy, but the diagnostic process can be long and AD can only be confirmed by an autopsy, during which pathologists look for the disease's characteristic plaques and tangles in brain tissue. The sooner an accurate diagnosis of “probable” AD is made, the easier it is to manage symptoms and plan for the future therapy. Therefore, statistical methods that can identify alterations in PET scans are an important component in the study and treatment in AD.

A number of statistical techniques have been developed to quantify various aspects related to PET neuroimaging. These techniques typically fall into one of two categories: analyses that focus on voxel- or region-wise differences in activity intensity; or analyses that highlight coordinated activity between voxels or regions in different areas of the brain. In the context of FDG, these techniques measure *metabolic activity* and *metabolic connectivity*, respectively. We provide an overview of statistical methods that have been used to analyze localized metabolic activity and connectivity using PET imaging. We then highlight one particular method that integrates both aspects and illustrating its performance on FDG PET scans from the Alzheimer's Disease Neuroimaging Initiative (ADNI).

2 | EXPERIMENTAL DATA

Data used in the preparation of this article were obtained from the ADNI database (adni.loni.usc.edu). The ADNI was launched in 2003 as a public–private partnership, led by Principal Investigator Michael W. Weiner, MD. The primary goal of ADNI has been to test whether serial magnetic resonance imaging (MRI), PET, other biological markers, and clinical and neuropsychological assessment can be combined to measure the progression of mild cognitive impairment (MCI) and early AD. For up-to-date information, see www.adni-info.org.

We use ADNI data to illustrate one of the methods reviewed in this article, examining FDG PET scans from groups of healthy controls (HCs), MCI, and AD patients taken at four successive time points. The tomographic reconstruction process of the PET projections ends with a three-dimensional (3D) array of activity values in a coordinate system specific to the individual being scanned. Typically, the reconstructed PET scan is coregistered to a T1-weighted anatomical MRI scan from the same subject. PET scans are generally relatively smooth, and functional PET scans generally do not reflect anatomical boundaries of the brain. The detail in the underlying T1 anatomical scan helps identify the relative location of the PET uptake values with respect to brain anatomy. The T1 MRI scan, in turn, is spatially transformed to best align with a T1 brain template defined in a standard stereotaxic coordinate system. Finally, that same spatial transformation is applied to the PET scan, interpolating uptake values to align with the standard brain anatomy. This transformation to standard space allows for voxel-wise comparison across subjects. Often, however, the PET uptake values within anatomically or functionally defined regions are averaged together, leading to a region-of-interest (ROI) representation with just one summary uptake value per region. The most commonly used stereotaxic coordinate system is known as MNI space by virtue of a brain template developed and provided by the Montreal Neurological Institute (Mazziotta et al., 1995). A number of different regional parcellations of the brain have been defined on the MNI template, but the automated anatomical labeling (AAL) parcellation (Tzourio-Mazoyer et al., 2002) is among the more popular. The number of voxels in a particular region can be quite large. For example, at a 2-mm isotropic grid, the number of voxels in the AAL parcellation range from 220 for the smallest feature (the amygdala) to 5104 (the middle frontal gyrus).

3 | STATISTICAL METHODS FOR THE ANALYSIS OF PET SCANS

FDG PET analyses typically fall under two distinct categories: metabolic activity and metabolic connectivity. Metabolic activity quantifies the FDG uptake rate in distinct brain locations (at a voxel or region level) and is generally regarded as providing a measure of distributed activity across the brain. Metabolic connectivity, on the other hand, quantifies the degree of association between brain region-pairs based on the consistency of FDG uptake across scans.

We review methods that focus on one or another of the two analyses and then examine an approach that integrates both.

3.1 | Statistical analysis of metabolic activity

Analyses of metabolic activity typically attempt to identify brain regions in patients with neurological disorders or dementia with abnormal uptake compared to HCs. Such approaches come in both voxel- and region-wise flavors.

Region-wise approaches generally involve *t*-tests or other linear analyses applied to regional summary measures derived from voxel intensities inside each region. Depending on the number of regions under consideration, corrections for multiple comparisons (e.g., Bonferroni) can be feasible. Examples of region-based analyses include Gray et al. (2012), which uses baseline, 12-month, and change over time as features for a support vector machine (SVM) classifier.

Similarly, statistical tests can be performed on a voxel-wise basis as well (Friston et al., 1995). For example, consider a voxel-wise general linear model (GLM) that characterizes the PET uptake in a region g from T scans of subject i. Let $T \times 1$ vector $\mathbf{Y}_{ig}(\nu)$ denote the FDG uptake at voxel ν in region g on T distinct scans (e.g., in the resting state and during the performance of a task) from subject i. The GLM models $\mathbf{Y}_{ig}(\nu)$ as a linear combination of the columns of the $T \times q$ design matrix $\mathbf{X}_i$, whose q columns consist, in the context of this survey, of indicator values that target a specific row of the dependent variable, and/or form contrasts between the rows, and, optionally, subject-dependent covariates; and a noise term $\epsilon_{ig}(\nu) \sim \mathrm{N}(\mathbf{0}, \sigma_{g\nu}\mathbf{I}_T)$:

$$\mathbf{Y}_{ig}(\nu) = \mathbf{X}_i \boldsymbol{\beta}_g(\nu) + \epsilon_{ig}(\nu),$$

where the $q \times 1$ effect vector $\boldsymbol{\beta}\,(\nu)$ characterizes the response.

In this basic form, the model above assumes that the FDG activity is voxel-wise independent. However, imaging data, and PET scans in particular, are generally smooth and nearby voxels are typically highly correlated, yet the GLM neglects to incorporate these correlations into estimates of the metabolic activity. As a consequence, this naive estimate reflects a mixture of the influence of neighboring voxels and the individual voxel activity. Incorporating an effect to model the influence of neighboring voxels results in a sharper estimate of the actual voxel activity itself. To this end, Bowman (2005) introduced a GLM that incorporates a spatial autoregressive component to account for the contributions of the voxels ν^* in the functional neighborhood N_ν that surrounds voxel ν. The model in Bowman (2005) consists of two stages, following the traditional approach to functional MRI (fMRI) analysis: first, fitting each subject's scans separately with design matrix $\mathbf{X}_i$, and then capturing spatial correlation across the fitted coefficients. Since PET studies generally have only a few scans per subject, we present a slightly modified model that combines the two stages:

$$\mathbf{Y}_{ig}(\nu) = \mathbf{X}_i \boldsymbol{\beta}_g(\nu) + \rho_g \frac{1}{|\mathcal{N}_\nu|} \sum_{\nu^* \in \mathcal{N}_\nu} \left(\mathbf{Y}_{ig}(\nu^*) - \mathbf{X}_i \boldsymbol{\beta}_g(\nu^*) \right) + \epsilon_{ig}(\nu),$$

where $|\mathcal{N}_\nu|$ denotes the $V_g - 1$ voxels in the functional neighborhood of voxel ν, and autoregressive parameter ρ_g, with $0 \le \rho_g < 1$, characterizes the degree of influence of neighboring voxels. This model reduces to the simpler, decoupled GLM above when $\rho_g = 0$.

Alternative models have been proposed to estimate metabolic activity while accounting for spatial correlations in the data (Bowman, 2007; Derado et al., 2013). The primary focus of these models is to estimate metabolic activity, and spatial correlations are captured to improve estimation of the metabolic activity by borrowing strength across voxels. For some models, robust estimation of the spatial correlations requires a large number of scans or subjects relative to the number of regions. Unfortunately, large-scale PET studies are extremely rare, thus limiting the number of regions that can be considered. We examine ways around this problem in the next sections.

Inferences can be drawn from these voxel-wise models, but given the large number of voxels involved, traditional corrections for multiple comparisons are untenable. PET images tend to have a relatively high degree of spatial correlation, or smoothness; the resulting lack of independence across voxels violates the assumptions underlying the rationale for traditional corrections for multiple comparisons. Friston et al. (1991) introduced the notion of a statistical parametric map (SPM), where the effect measured (e.g., group mean difference) is replaced by a test statistic characterizing that effect. Using elements of random field theory, they derived a smoothness adjustment to the voxel-wise distribution of the null hypothesis to account for the lack of independence from neighboring voxels. For a desired level of significance α, the adjustment induces a reciprocal relationship between the the number of voxels N and the per-voxel test statistic threshold that is far less stringent than those dictated by traditional correction methods. In practice, due to the smoothness of the PET image, the thresholding of the SPM results in 3D “islands,” or clusters, of locally adjacent voxels. Clusters whose number of voxels exceeds the lower bound on N established by the smoothing adjustment are deemed significant. In this way, SPMs provide an alternate, more realistic approach to account for the multiple comparisons that inevitably arise in voxel-wise analyses.

We note that a recent analysis in the fMRI community has called into question the assumptions used to derive the smoothness adjustment (Eklund et al., 2016), citing failure to control cluster family wise error to the desired level α. Similar issues may apply to PET findings as well (Ganz et al., 2020).

A number of studies have employed SPMs. Using a SPM-based approach in a longitudinal setting, Gray et al. (2012) devised an SVM-based classifier using average uptake values from 83 regions at two different time points to differentiate between HC, stable and progressing MCI, and AD patients. In a similar longitudinal analysis, Rodrigues and Silveira (2014) evaluated SVM classification performance between a region-wise and voxel-wise approach; they found that the greater number of features afforded by the voxel-wise approach gave higher classification accuracy than that base on regions. Patterson et al. (2011) employed SPM analysis to identify clusters with significantly different FDG uptake between AD and MCI patients as a way to identify patterns of potential onset of AD.

3.2 | Statistical analysis of metabolic connectivity

Multiple statistical techniques have been applied to the calculation and analysis of metabolic connectivity (Yakushev et al., 2017), including studies specifically targeting AD (Morbelli et al., 2013; Rahmani et al., 2020). We note that, unlike fMRI for example, PET studies typically generate just one scan per subject. So, while inter-region correlation of fMRI activity can be computed on a per-subject basis by correlating regional values across time, in PET this is generally not an option. As such, measuring similarity of uptake between regions is typically performed on an ensemble of subjects, either over the entire cohort or on a per-group basis depending on the analysis. However, some newer techniques have been developed that allow for the computation of metabolic connectivity on a per-subject basis based on specific assumptions about the behavior of uptake. Methods generally break down into some combination of the following categories:

3.2.1 | Inter-regional correlation analysis

One basic form of inter-regional correlation analysis consists of correlating across subjects the uptake of a particular voxel of interest with that of all other voxels in the brain. This so-called seed region approach highlights regions of the brain that have similar uptake patterns as the seed region (Metter, Riege, Kameyama, et al., 1984; Metter, Riege, Kuhl, et al. 1984). Lee et al. (2008) characterized the nature of voxel-wise correlations within a particular ROI, indicating if a given voxel in the region generated correlation only within said region, or extended to the region's contralateral counterpart, or if significant (as determined by SPM) regions of voxels at other locations showed strong association. Carbonell et al. (2014) developed a hierarchy of hypotheses designed to classify between-group differences in the variance–covariance characteristics relating the seed voxel uptake pattern to that in other voxel locations in the brain. Their technique successively identifies regions with group differences in correlation; or group differences in variance or covariance; or regions with proportional variance–covariance structure between groups. Chung et al. (2016) examined differences in metabolic connectivity between early- and late-onset AD. Expanding from the simple seed-region approach, they estimated full AAL-based region-to-region correlation matrices for each group. They generated 10,000 such matrices per group based on subject resamplings, then used nonparametric permutation tests to identify region pairs with significant connectivity differences between the groups. They estimated full AAL-based region-to-region correlation matrices for each group, and computed correlation differences between groups, using nonparametric permutation tests to identify significant differences.

3.2.2 | Sparse inverse covariance estimation

As a precursor to sparse inverse covariance estimation (SICE), Horwitz et al. (1984) proposed to analyze the metabolic connectivity by identifying region-pairs with strong associations. However, they found that the large intersubject variability in global whole brain uptake rate induced significant ($p < 0.01$) correlations between every region pair. To eliminate this nonspecific effect, they examined associations between region pairs using *partial* correlations with respect to the global uptake rate between regions. In subsequent work, Horwitz et al. (1987) acknowledged that even a few outliers could have an outsized impact on a correlation's parametrically derived p-value. To make their selection process more robust, they adopted a series of criteria based on idempotent, jackknife, and bootstrap resamplings to identify “reliable” region pair associations. They then applied the technique to AD patients and HCs to examine differences in connectivity.

The actual SICE approach (Friedman et al., 2007), also known as the Graphical Lasso, works in the inverse covariance domain where partial correlations between a given region-pair represent the direct association of uptake between the two regions independent of any indirect contributions via other regions. SICE leverages an L1-penalized maximum likelihood estimator of the inverse covariance matrix $\mathbf{\Theta} = \mathbf{\Sigma}^{-1}$, maximizing:

$$\log\det\mathbf{\Theta} - \mathrm{tr}(\mathbf{S}\mathbf{\Theta}) - \lambda\|\mathbf{\Theta}\|_1,$$

where $\mathbf{S}$ is the sample covariance matrix. Increasing the penalization strength via regularization parameter λ leads to fewer region-pairs with nonzero partial correlations, but increases the bias of the correlations that remain.

Both Huang et al. (2010) and Titov et al. (2016) leveraged the variable selection properties of SICE to identify region pairs with nonzero partial correlation. However, acknowledging the bias introduced by SICE on those nonzero estimates, both researchers employed subsequent constrained estimation of the nonzero partial correlations via Dempster (1972). Huang et al. (2010) used this SICE approach to estimate covariance matrices for HCs, MCI patients, and AD patients, and then used these covariance matrices in classifiers to determine which group a new pattern of uptake values most likely belonged. Similarly, Titov et al. (2016) formed maximum-likelihood framework to differentially classify HCs, mild AD patients, and patients with mild frontotemporal lobar degeneration. The choice of regularization parameter λ, which governs the sparsity of the estimated partial covariance matrix, differed between their approaches: Huang et al. (2010) adjusted λ to target a prespecified number of nonzero connections between region pairs (e.g., 60, 120, 180). Titov et al. (2016), in contrast, employed a maximum a posteriori probability estimator proposed by Bani Asadi et al. (2009) to jointly estimate λ and the sparse inverse covariance matrix. Although comparison of classification performance between the two approaches is hindered by the use of nonidentical cohorts and different subset of ROIs, the approach of Titov et al. (2016) correctly distinguished between HC and AD patients with 96%, compared to 88% with Huang et al. (2010).

3.2.3 | Principal and independent component analysis

A number of statistical techniques have been used to identify spatial patterns of voxels that have similar spatial FDG uptake profiles across subjects, notably principal component analysis (PCA) (Jolliffe & Cadima, 2016) and independent component analysis (ICA) (Stone, 2002). A variant of PCA known as the subprofile scaling model (SSM) (Alexander & Moeller, 1994; Moeller et al., 1987), in particular, has seen extensive use in the PET domain: SSM's initial conditioning of the data matrix, including initial log transformation of the data followed by both row and column centering, is well suited as a preprocessing step for the strictly positive PET measurements. ICA, in the context of imaging, comes in two flavors: spatial-ICA (sICA) and temporal-ICA (tICA) (so named due to its origins in the blind source separation of time series signals). The tICA flavor has little application in the PET context given that the nonspatial dimension of the data matrix in the PET context is “subjects.” In both sICA and PCA, each 3D scan is converted to a 1D row vector of length p; then these row vectors are stacked to form a n (subjects) $\times$ p (voxels) matrix of uptake values. Typically, the columns of this matrix are shifted to have zero mean (though, as noted, SSM-PCA performs more complex initial conditioning), giving data matrix $\mathbf{D}$.

Although the underlying methodologies vary, both PCA and sICA model the data matrix in a similar fashion:

$$\mathbf{D} = \mathbf{S} \times \mathbf{V}^T,$$

where the columns of $\mathbf{V}$ represent spatial decomposition of the data matrix, and $\mathbf{S}$ describes how those patterns are combined to reconstitute the data matrix. In PCA, the columns of $\mathbf{V}$ form the principal components and each row of $\mathbf{S} = \mathbf{U} \times \mathbf{\Lambda}$ provides the coordinates of the corresponding subjects scan on the basis defined by $\mathbf{V}$. In sICA, the columns of $\mathbf{V}$ are considered realizations of random variables whose underlying distributions are non-Gaussian and mutually maximally independent from each other, and $\mathbf{S}$ is known as the mixing matrix. In both approaches, any anatomically defined ROIs that have significant overlap with an identified component are often considered to form a network: they are all associated by the characteristics that defined the component. For example, in resting-state fMRI, one frequently identified ICA component is called the default mode network consisting of the medial prefrontal cortex, the posterior cingulate cortex/precuneus, and the angular gyrus. Each FDG uptake scan can be decomposed onto these spatial patterns, giving a set of scores that can be used for classification purposes. Eidelberg (2009) reviews the use of SSM in the realm of metabolic connectivity to identify patterns associated with various disease states.

A number of so-called multimodal extensions to ICA have been developed to relate patterns across distinct data sets; see Yang et al. (2021) for an overview. These extensions range from joint ICA (Calhoun, Adali, Giuliani, et al., 2006; Calhoun, Adali, Kiehl, et al. 2006) to parallel ICA (Liu et al., 2009) and linked ICA (Groves et al., 2011), to multimodality concatenated ICA (Li et al., 2021), each uncovering increasingly sophisticated relationships between the supplied modalities.

In terms of applications of these methods, many researchers have used the spatial bases derived from these techniques to discriminate between distinct groups. Approaches vary, from relying on the first principal component as the separator (Alexander & Moeller, 1994; Pagani et al., 2009), to more sophisticated approaches (Scarmeas et al., 2004) that form linear combination of the principal components to as the separating hyperplane. Toussaint et al. (2012) identified components using both SPM and ICA analyses and devised support vector machines (SVM) to distinguish stable MCI subjects from those at risk of conversion to AD. Likewise, Pagani et al. (2016) applied sICA to FDG scans of amyotrophic lateral sclerosis patients and HCs, and similarly used the resulting coordinates system to separate the groups. Laforce et al. (2014) applied parallel ICA to jointly analyze PET-FDG and PET-PIB in the context of AD.

3.2.4 | Graph theory

Graph theoretic analyses (Bullmore & Sporns, 2009) are typically performed after the estimation of the correlation matrix. The correlation matrix is converted to a binary adjacency matrix (e.g., via thresholding or SICE), effectively defining a finite graph. Then summary characteristics of the graph (such as characteristic path length, small world properties, etc.) can be extracted and compared. Veronese et al. (2019) used a graph theoretic approach for the quantification of FDG covariance and defined an entropy metric relevant for AD to show an association with the progression of the pathology. Spetsieris and Eidelberg (2021) performed SICE on the anatomical ROIs within the SSM network that most differentiates disease status from HCs; bootstrapping samples over a range of sparsity, they use eigenvalue centrality measures on the resulting adjacency matrices to identify the ROIs in the discriminating network whose connectivity is most robust.

3.2.5 | Single-subject estimates of metabolic connectivity

The methods discussed so far compute metabolic connectivity by deriving statistics across a collection of scans. The methods in this section are novel in that they estimate a measure of connectivity *for each individual subject*. Huang et al. (2020) proposed an element-wise, region-pair adjustment to a group-derived correlation matrix from HC subjects. The element-wise adjustment relies on an effect-size normalization of the between-region differences in activity between the individual PET scan and the average HC group activity. In their derivation, a large effect of region-pair difference in uptake leads to a shrinking of the HC group correlation for the corresponding region-pair. Another approach, the Kullback–Leibler divergence similarity estimation (KLSE), does not rely on the adjustment of predefined correlation matrix. Instead, Wang et al. (2020) posited that brain regions with similar distributions of voxel intensities indicate a common underlying metabolic process. They defined a similarity measure using Kullback–Leibler (KL) divergence to estimate the similarity of voxel intensity distributions pairwise between regions.

Given probability distributions P and Q of voxel intensities for two different regions, the similarity measure is defined as

$$S_{\mathrm{KL}}(P,Q) = \exp(-D_{\mathrm{KL}}(P,Q)),$$

with the Kullback–Leibler divergence expressed as

$$D_{\mathrm{KL}}(P,Q) = \int_x P(x)\log\frac{P(x)}{Q(x)} + Q(x)\log\frac{Q(x)}{P(x)}dx,$$

providing a symmetric (undirected) estimate of connectivity between the two regions. Applied to all region-pairs, this technique generates a connectivity matrix representative of one particular scan. Wang, Yan, et al. (2020) used KLSE to characterize the connectivity patterns between stable and progressive MCI patients using the AAL parcellation. Comparing the patterns of stable and progressive MCI patients they were able to identify a difference pattern that implicated regions associated with conversion to AD. Using this pattern, they devised a classifier that outperformed discriminators based on ROI-based mean intensity values as well as the distribution of voxel intensities within a spatial component associated with conversion to AD derived from spatial covariance analysis.

3.3 | Joint analysis of metabolic activity and connectivity: A Bayesian spatial model

As summarized above, many different techniques have been developed to characterize either metabolic activity or metabolic connectivity in the brain. To our knowledge, only one approach has been developed to characterize jointly metabolic activity *and* metabolic connectivity. In what follows, we apply an updated version of a Bayesian spatial model for activation and connectivity (BSMac) (Bowman et al., 2008) to quantify FDG-derived metabolic characteristics of the brain. The update accommodates the inclusion of covariates to control of age, socioeconomic status, handedness, and other potentially confounding variables; also, the model has been extended to permit as many regions as one wishes, even with a limited sample size—with the caveat that the number of inter-regional correlation estimates remains constrained by the sample size. Unlike the approaches above, ours is the first unified approach that integrates the elements of metabolic activity (at the voxel level) and metabolic connectivity (at the regional level) into a single model. Our integrated approach thus provides self-consistent modeling of the metabolic characteristics of the brain.

To illustrate the capabilities of our model, we employed FDG scans from healthy, cognitively normal controls (HC, $n = 69$), MCI ($n = 125$), and AD ($n = 53$) patients across four different time points (baseline, 6, 12, and 24 months) from ADNI to estimate the model parameters, and then used the model to derive inferences about activity and connectivity among the three groups. Covariates included in the model were age, weight, and the cognitive subscale of the Alzheimer's Disease Assessment Scale, each standardized to z-scores across all subjects.

BSMac, implemented as a MATLAB toolbox (Zhang et al., 2012), performs parameter estimation based on Markov chain Monte Carlo (MCMC) methods and generates plots for activation and connectivity (Derado et al., 2012; Zhang et al., 2012). The toolbox includes several extensions to the original Bowman et al. (2008) model, for example, incorporating covariate effects into the spatial model and implementing analyses for small sample sizes. BSMac is released as an open-source package under the GNU public license (http://www.gnu.org/licenses/gpl.html) and is available upon request to the authors.

Our analysis uses FDG scans preprocessed through Step 4 of the ADNI preprocessing protocol (http://www.loni.ucla.edu/ADNI). To summarize, the scans from each subject's visits are coregistered in native, aligned to the anterior to posterior commisure line on a standard voxel grid, intensity normalized to a mean value of one within the subject's brain mask, and smoothed to an isotropic resolution of 8 mm full width at half maximum. We subsequently determined an affine, 12 degrees of freedom transform that best warp the subject's averaged intensity-normalized scans to stereotaxic MNI space by way of a PET-FDG template. The four intensity-normalized scans were warped to MNI space by means of this transform. Finally, each spatially normalized scan was scaled in intensity so that the mean intensity of the upper cerebellum (whose FDG uptake is thought to be insensitive to age and cognitive status) equals one for improved comparison across groups and visits (Rasmussen et al., 2012).

3.3.1 | Model

Let $i = 1, 2, \ldots, K$ index subjects, and j denote specific group × visit combinations: each subject belongs to one of three groups (HC, MCI, or AD) and has four scans (baseline and three subsequent visits). BSMac leverages a parcellation of the brain into regions defined in MNI space, such as those proposed by the AAL (Tzourio-Mazoyer et al., 2002) or the Brodmann maps (Judaš et al., 2012). The G regions are indexed by $g = 1, 2, \ldots, G$, and contain V_g voxels; intensity values from all voxels in region g are stacked into a single vector.

$\mathbf{Y}_{igj}$ denotes the average FDG uptake for subject i in region g for group × visit combination j. (Note that here $\mathbf{Y}_{igj}$ is a vector of length V_g, with one element per voxel, in contrast to the vector of scans $\mathbf{Y}_{ig}(\nu)$ at voxel ν in the GLM model presented earlier.) Finally, let x_{iq} represent the qth ($q = 1, 2, \ldots, Q$) covariate for subject i.

The BSMac model has the following hierarchical structure:

$$\begin{array}{rl}
\mathbf{Y}_{igj} \mid \boldsymbol{\mu}_{gj}, \alpha_{igj}, \boldsymbol{\eta}_{gjq}, \sigma^2_{gj} \sim \mathrm{MVN}\left(\boldsymbol{\mu}_{gj} + \mathbf{1}\alpha_{igj} + \sum_{q=1}^{Q} \boldsymbol{\eta}_{gjq} x_{iq}, \sigma^2_{gj}\mathbf{I}\right); & \\
 & \sigma^{-2}_{gj} \sim \mathrm{Gamma}(a_0, b_0) \\
\boldsymbol{\mu}_{gj} \mid \lambda^2_{gj} \sim \mathrm{MVN}\left(\mathbf{1}\mu_{0gj}, \lambda^2_{gj}\mathbf{I}\right) & \lambda^{-2}_{gj} \sim \mathrm{Gamma}(c_0, d_0) \\
\boldsymbol{\eta}_{gjq} \mid \tau^2_{gjq} \sim \mathrm{MVN}\left(\mathbf{0}, \tau^2_{gjq}\mathbf{I}\right) & \tau^{-2}_{gjq} \sim \mathrm{Gamma}\left(e_{0q}, f_{0q}\right) \\
\boldsymbol{\alpha}_{ij} \mid \boldsymbol{\Gamma}_j \sim \mathrm{MVN}\left(\mathbf{0}, \boldsymbol{\Gamma}_j\right) & \boldsymbol{\Gamma}_j^{-1} \sim \mathrm{Wishart}\left\{\left(h_0 \mathbf{H}_{0j}\right)^{-1}, h_0\right\}
\end{array} \qquad (1)$$

where $\boldsymbol{\mu}_{gj} = (\mu_{gj}(1), \ldots, \mu_{gj}(V_g))'$, $\boldsymbol{\eta}_{gjq} = (\eta_{gjq}(1), \ldots, \eta_{gjq}(V_g))'$, and $\boldsymbol{\alpha}_{ij} = (\alpha_{i1j}, \ldots, \alpha_{iGj})'$. Parameter μ_{0gj} denotes the mean voxel intensity in region g across all subjects in Group × Visit combination j. The $G \times G$ matrix $\mathbf{H}_{0j}$ is the sample covariance matrix of the mean regional values in Group × Visit combination j. The model assumes that each individual's normalized glucose uptake at the voxel level is randomly distributed around a population (or group) parameter, $\boldsymbol{\mu}_{gj}$, plus an individualized region-specific random effect, $\mathbf{1}\alpha_{igj}$, after adjusting for covariate effects through $\boldsymbol{\eta}_{gjq}$. The regional random effect α_{igj}, the gth element of vector $\boldsymbol{\alpha}_{ij}$, contributes to short range intra-regional correlations and accounts for possible long-range inter-regional spatial correlations through the covariance matrix $\boldsymbol{\Gamma}_j$. We define the mean regional uptake θ_{gj} as the mean value of the V_g elements of $\boldsymbol{\mu}_{gj}$. For more details on the model specification and the explanation of the correlation structure, see Zhang et al. (2012).

3.3.2 | Inference

For estimation, we use MCMC method with the Gibbs sampler. BSMac's Gibbs-friendly model specification facilitates estimation by providing substantial reductions in computing time and memory. After discarding iterations included in the burn-in period, the computing time and memory can be further reduced with a thinning factor, which retains samples from the joint posterior distribution drawn at the specified interval. For this analysis, BSMac MCMC estimation was set up with a burn-in of 1000 samples, followed by a 6000 sample run with a thinning factor of 10, resulting in $D = 600$ draws indexed by $d = 1, 2, ..., D$. Relatively uninformative priors were specified via hyperparameters $a_0 = 0.1$, $b_0 = 0.005$, $c_0 = 0.1$, $d_0 = 0.010$; $e_{0q} = 0.1$, and $f_{0q} = 0.05 \; \forall \; q$. Parameter h_0 denotes the Wishart degrees of freedom, equal to the number of subjects in Group × Visit combination j.

3.3.3 | Inference of regional FDG uptake

Once the BSMac model parameters outlined in 1 have been estimated, the MCMC process via Gibbs sampling generates near-independent samples of voxel-level uptake, $\boldsymbol{\mu}_{gj}$; regional-level uptake, θ_{gj}; and inter-region correlation, $\boldsymbol{R}_j = \boldsymbol{\Lambda}_j{}^{-1}\boldsymbol{\Gamma}_j\boldsymbol{\Lambda}_j{}^{-1}$, where diagonal matrix $\boldsymbol{\Lambda}_j = \mathrm{diag}(\boldsymbol{\Gamma}_j)^{12}$.

In the exposition that follows, we use the regional uptake values θ_{gj} to outline the inference procedure, but the procedure itself can be applied element-wise to $\boldsymbol{\mu}_{gj}$ and $\mathbf{R}_j$ as well.

We denote by θ_{gjd} the regional activation produced by the dth draw of D total draws from the MCMC procedure. To examine differences in regional uptake between groups, visits, or both, we introduce contrast sequence c_j, $j = 1, 2, ..., J$, with coefficients chosen to isolate and contrast desired combinations of Group × Visit scans of interest, and collapse across j:

$$\theta_{gcd} \overset{(\mathrm{def})}{=} \sum_{j=1}^{J} c_j \theta_{gjd}. \tag{2}$$

Let indicator function $I_+(x) = 1$ when $x > 0$, 0 otherwise. We use the following as the estimator of the probability that the contrasted FDG uptake region g exceeds threshold δ:

$$\begin{aligned} P_\delta^+\left(\theta_{gc}\right) &\overset{(\mathrm{def})}{=} \frac{1}{D}\sum_{d=1}^{D} I_+\left(\theta_{gcd} - \delta\right) \\ &\approx \Pr\left(\theta_{gc} > \delta\right). \end{aligned} \tag{3}$$

In a similar manner, we can define $P_\delta{}^-(\theta)_{gc}$, an estimator for $\Pr(\theta_{gc} < -\delta)$.

3.3.4 | Metabolic connectivity

The BSMac model enables inferences about the associations of FDG uptake between region-pairs based on samples $\{\boldsymbol{\Gamma}_{jd} \mid d = 1, 2, ..., D\}$ generated by the MCMC process. We apply concepts outlined above to form contrasts on each region-pair element of $\boldsymbol{\Gamma}_{jd}$ and draw inferences by examining exceedance probabilities formulated from the empirical distribution of each. We also estimate the posterior median correlation matrix of the set of correlation matrix draws using a two-step procedure. First, we determine the posterior median covariance matrix (the point on the manifold of symmetric positive semi-definite matrices that minimizes the sum of distances to covariance matrix draws $\{\mathbf{\Gamma}_{jd} \mid d = 1, 2, ..., D\}$) (Fletcher et al., 2008). Then, we project the result onto the submanifold of positive symmetric difference matrices with unit diagonal by pre- and post-multiplying by the appropriately scaled diagonal matrix, as noted above. (Note that we have opted for this estimation approach because efficient methods to directly compute the median correlation matrix do not currently exist.) Finally, we determine, element-wise, the region-pair contrasts across groups and visits as dictated by the contrast coefficients c_j.

3.3.5 | Contrasts

Our data set consists of three groups of patients (HC, MCI, and AD) scanned over four visits (Baseline, Month 6, Month 12, and Month 24). In the model, the 12 basic Group × Visit combinations are enumerated by the single index $j = 1, 2, ..., 12$. The contrast sequence c_j dictates how these 12 scans are combined to form quantities of interest, typically differences between groups, visits, or a combination of both. We introduce a bracket-based notation to help classify and refer to different types of contrasts used throughout the remainder of the paper. We refer to the different sets as "blocks," visualized as outer products of group and visit differences. The different categories of contrasts are:

- a three-by-four block of zero-difference, base contrasts which we label $\langle\cdot\rangle \times \langle\cdot\rangle$ (e.g., $\langle\text{HC}\rangle \times \langle\text{Baseline}\rangle$);
- a three-by-three block of single-difference contrasts highlighting the change over time relative to the baseline visit for each individual group, summarized as $\langle\cdot\rangle \times \langle-\rangle$ (e.g., $\langle\text{HC}\rangle \times \langle\text{24 Months} - \text{Baseline}\rangle$);
- a three-by-four block of single-difference contrasts comparing between-group differences at a given visit, summarized as $\langle-\rangle \times \langle\cdot\rangle$ (e.g., $\langle\text{AD} - \text{HC}\rangle \times \langle\text{Baseline}\rangle$); and
- a three-by-three block of double-difference contrasts that quantify how a particular group difference changes over time, summarized as $\langle-\rangle \times \langle-\rangle$ (e.g., $\langle\text{AD} - \text{HC}\rangle \times \langle\text{24 Months} - \text{Baseline}\rangle$).

This block structure will become apparent in later graphics.

4 | RESULTS

We select $G = 52$ AAL regions (Tzourio-Mazoyer et al., 2002) from among the frontal, temporal, and parietal lobes, as well as subcortical gray matter structures, deemed relevant to AD pathology. (The selected regions appear in Figure 2.)

4.1 | Metabolic activity

Table 1 lists regions that contain greater than 50% of voxels whose between-group difference in $\langle\text{24 Months} - \text{Baseline}\rangle$ change in uptake is very probably positive ($P_{\delta=0}{}^{+}(\mu) > 0.90$) or negative ($P_{\delta=0}{}^{-}(\mu) > 0.90$). In two of the three group differences, the 50% threshold was exceeded by voxels with high probability of being negative. Seven such regions were found for $\langle\text{AD} - \text{MCI}\rangle \times \langle\text{24 Months} - \text{Baseline}\rangle$; a superset with nearly twice as many regions was found for $\langle\text{AD} - \text{HC}\rangle \times \langle\text{24 Months} - \text{Baseline}\rangle$. No regions had sufficient number of voxels with $P_{\delta=0}{}^{+}(\mu) > 0.90$. Also, for the remaining group difference, no regions for the $\langle\text{MCI} - \text{HC}\rangle \times \langle\text{24 Months} - \text{Baseline}\rangle$ met the selection criteria.

The table also indicates the corresponding probability of aggregate regional $\langle\text{24 Months} - \text{Baseline}\rangle$ change, both for the group differences and for each group individually. For the $\langle\text{AD} - \text{MCI}\rangle$, $\langle\text{AD} - \text{HC}\rangle$, and the AD cases, these regional probabilities are uniformly zero (i.e., none of the MCMC draws gave an aggregate regional value greater than zero); the probabilities for $\langle\text{MCI}\rangle \times \langle\text{24 Months} - \text{Baseline}\rangle$ are all similarly small. In contrast, the regional probabilities of the $\langle\text{HC}\rangle \times \langle\text{24 Months} - \text{Baseline}\rangle$, however, range from relatively low (≈ 0.2) to quite high (0.9).

Figure 1 indicates voxels with high or low probabilities for the three group difference changes on a backdrop of the brain. Following the pattern noted in Table 1, both $\langle\text{AD} - \text{HC}\rangle \times \langle\text{24 Months} - \text{Baseline}\rangle$ and $\langle\text{AD} - \text{MCI}\rangle \times \langle\text{24 Months} - \text{Baseline}\rangle$ exhibit large numbers of voxels with low probability of the corresponding contrast exceeding zero (indicated in blue). The $\langle\text{MCI} - \text{HC}\rangle \times \langle\text{24 Months} - \text{Baseline}\rangle$ case, however, displays far fewer voxels with such low probability contrasts.

In short, we infer that AD and MCI exhibit similar patterns of decline in FDG uptake, with said decline more severe for AD than MCI. HC, in contrast, does not exhibit such a decline.

4.2 | Metabolic connectivity

We explore the association of FDG uptake between region-pairs in two ways. In the first approach, we form contrasts directly on the individual MCMC-derived correlation draws, and then infer connectivity strength via the resulting empirical cumulative distribution. In the second approach, we determine the posterior median matrix for each group-

TABLE 1 Bayesian spatial model for activation and connectivity (BSMac)-inferred voxel- and region-level change in uptake. The between-group differences by ⟨24 Months − Baseline⟩ change (left) indicate for each region the percentage of voxels (VPct) for which $\text{Pr}_{\delta=0}{}^{+}(\cdot) < 0.01$. Only regions for which VPct exceeded 50% are shown here. Note that at this threshold, no regions had more than 50% of voxels with $\text{Pr}_{\delta=0}{}^{+}(\cdot) > 0.90$. Secondary values, VAbs and RPr indicate the corresponding absolute number of voxels (VAbs) and the region-level $P_{\delta}{}^{+}(\theta)$ (RPr). The ⟨24 Months − Baseline⟩ change in uptake for each group individually (right) is summarized by regional RPr (i.e., $P_{\delta=0}{}^{+}(\theta)$ for the corresponding region). Red values indicate regions that, for a particular between-group difference in change in uptake, show highly probable pair-wise association with another region at $p > 0.90$; see Table 2.

	AD − MCI			MCI − HC			AD − HC			AD	MCI	HC
Region	VPct	VAbs	RPr	VPct	VAbs	RPr	VPct	VAbs	RPr	RPr	RPr	RPr
Regional—Negative												
Voxel—Negative												
Temporal Mid (R)	88.6	3851	0				91.2	3965	0	0	0.000	0.213
SupraMarginal (R)	78.0	1540	0				83.5	1648	0	0	0.258	0.885
Frontal Mid (R)	51.4	2519	0				80.4	3939	0	0	0.000	0.413
Temporal Inf (R)	77.9	2750	0				79.2	2798	0	0	0.005	0.297
Temporal Mid (L)	72.3	3569	0				70.1	3463	0	0	0.005	0.227
Temporal Inf (L)	65.3	2086	0				69.8	2231	0	0	0.012	0.335
Frontal Inf Tri (R)							65.9	1201	0	0	0.000	0.798
Frontal Inf Oper (R)							60.8	789	0	0	0.010	0.857
Temporal Sup (R)							60.7	1852	0	0	0.020	0.632
Temporal Sup (L)	55.4	1272	0				58.6	1345	0	0	0.037	0.390
Frontal Mid (L)							57.2	2745	0	0	0.000	0.173
Frontal Inf Tri (L)							56.7	1407	0	0	0.000	0.360
SupraMarginal (L)							56.0	703	0	0	0.170	0.657

Abbreviations: AD, Alzheimer's disease; HC, healthy control; MCI, mild cognitive impairment.

by-visit combination j from the corresponding MCMC draws of the inverse variance–covariance matrix $\{\boldsymbol{\Gamma}_{jd}\}_{d=1}{}^{D}$. Then we form contrasts directly on elements of the posterior median to examine differences in group, visit, or both. Both approaches provide insight into the strength of association of metabolic activity between region pairs.

4.2.1 | Via Bayesian inference

Figure 2 uses connectograms to highlight strongly probable positive and negative associations between region pairs for two (single-difference) contrasts: ⟨*HC*⟩ × ⟨24 Months − Baseline⟩ and ⟨*AD*⟩ × ⟨24 Months − Baseline⟩. Here, contrasted region-pair correlations determined to be positive or negative with 90% probability or greater are shown as color-coded arcs connecting the two regions. In addition to connectivity, the figure also quantifies regional FDG uptake by presenting the probability of positive (red) and negative (blue) uptake in nested outer rings. Finally, the regions are grouped into sectors based on their membership in various anatomical brain structures.

In terms of connectivity, 14 region-pairs exhibited highly probable positive contrasts exceeding 90% for contrast ⟨HC⟩ × ⟨24 Months − Baseline⟩. Regions in the left parietal lobe and right temporal lobe garnered the majority of connection endpoints. (See Figure 3 for an explicit accounting of connection endpoints.) Contrast ⟨AD⟩ × ⟨24 Months − Baseline⟩, however, showed no correlation contrasts with sufficiently consistent positive or negative values to reach the 90% threshold.

In terms of activity, ⟨HC⟩ × ⟨24 Months − Baseline⟩ has five regions with greater than 90% probability of increase in uptake from Baseline to Month 24, three of which were found in the right frontal lobe. The caudate, bilaterally, shows greater than 90% probability of decrease in activity from Baseline to Month 24. For ⟨AD⟩ × ⟨24 Months − Baseline⟩, however, virtually all regional activations were found to decrease from Baseline

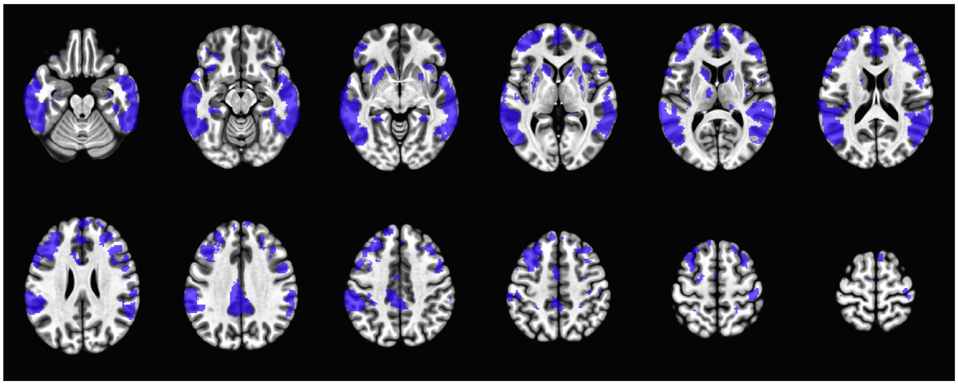

(a) $\langle \text{AD} - \text{MCI} \rangle \times \langle \text{Month 24} - \text{Baseline} \rangle$

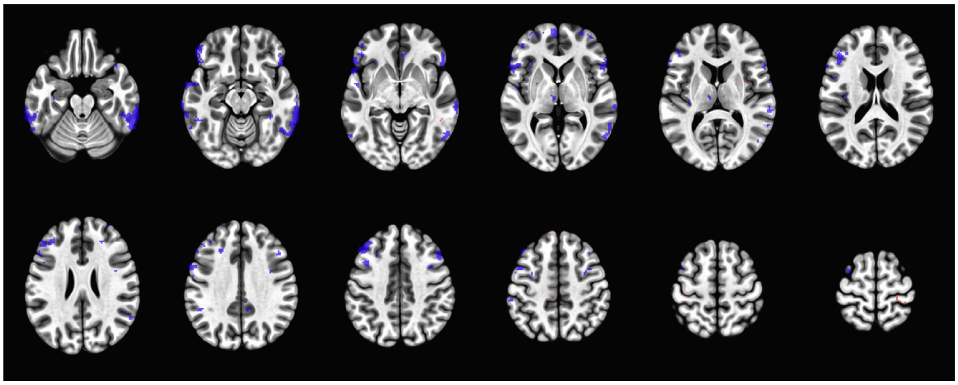

(b) $\langle \text{MCI} - \text{HC} \rangle \times \langle \text{Month 24} - \text{Baseline} \rangle$

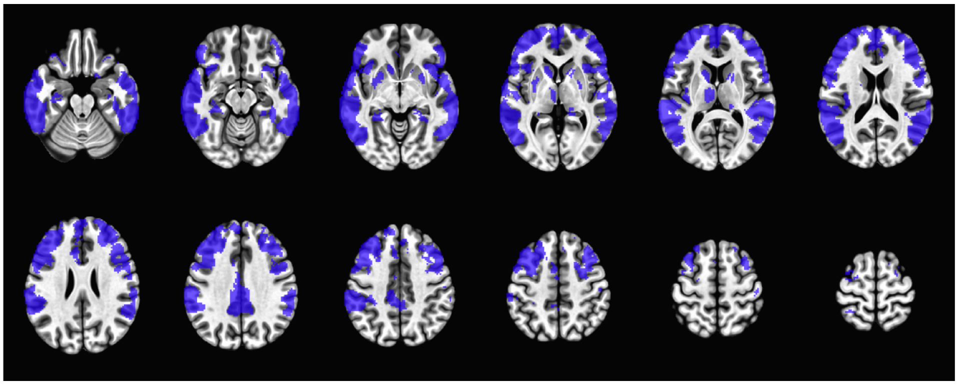

(c) $\langle \text{AD} - \text{HC} \rangle \times \langle \text{Month 24} - \text{Baseline} \rangle$

FIGURE 1 The Bayesian spatial model for activation and connectivity (BSMac)-inferred between-group voxel-wise differences in the $\langle \text{Month 24} - \text{Baseline} \rangle$ change in uptake. Colored voxels signal that, with high probability, the contrast is positive ($P_{\delta=0}{}^{+}(\mu) > 0.90$ in red) or negative ($P_{\delta=0}{}^{-}(\mu) > 0.90$ in blue).

to Month 24 with probability one. Only the pallidum, bilaterally, shows a hint of probable non-negative increase over time, but not sufficient to reach the 90% threshold.

For a more complete picture, Figure 3 shows the full array of connectograms in a fashion similar to Figure 2. Although anatomical sector labels and region names have been removed, this figure includes the number of connections terminating at each anatomical sector. Also, in some blocks the posterior distributions used to compute connectivity results have been altered by increasing threshold δ used to compute $P_{\delta}{}^{+}(\rho)$ and $P_{\delta}{}^{-}(\rho)$. For the three-by-four $\langle \cdot \rangle \times \langle \cdot \rangle$ block of elemental correlations, $\delta = 0.5$, and for the three-by-three $\langle - \rangle \times \langle \cdot \rangle$ group-difference contrasts, $\delta = 0.1$. In the remaining two blocks, $\delta = 0$. Without these nonzero thresholds, the pervasive connectivity in these blocks completely drowns out any interesting patterns.

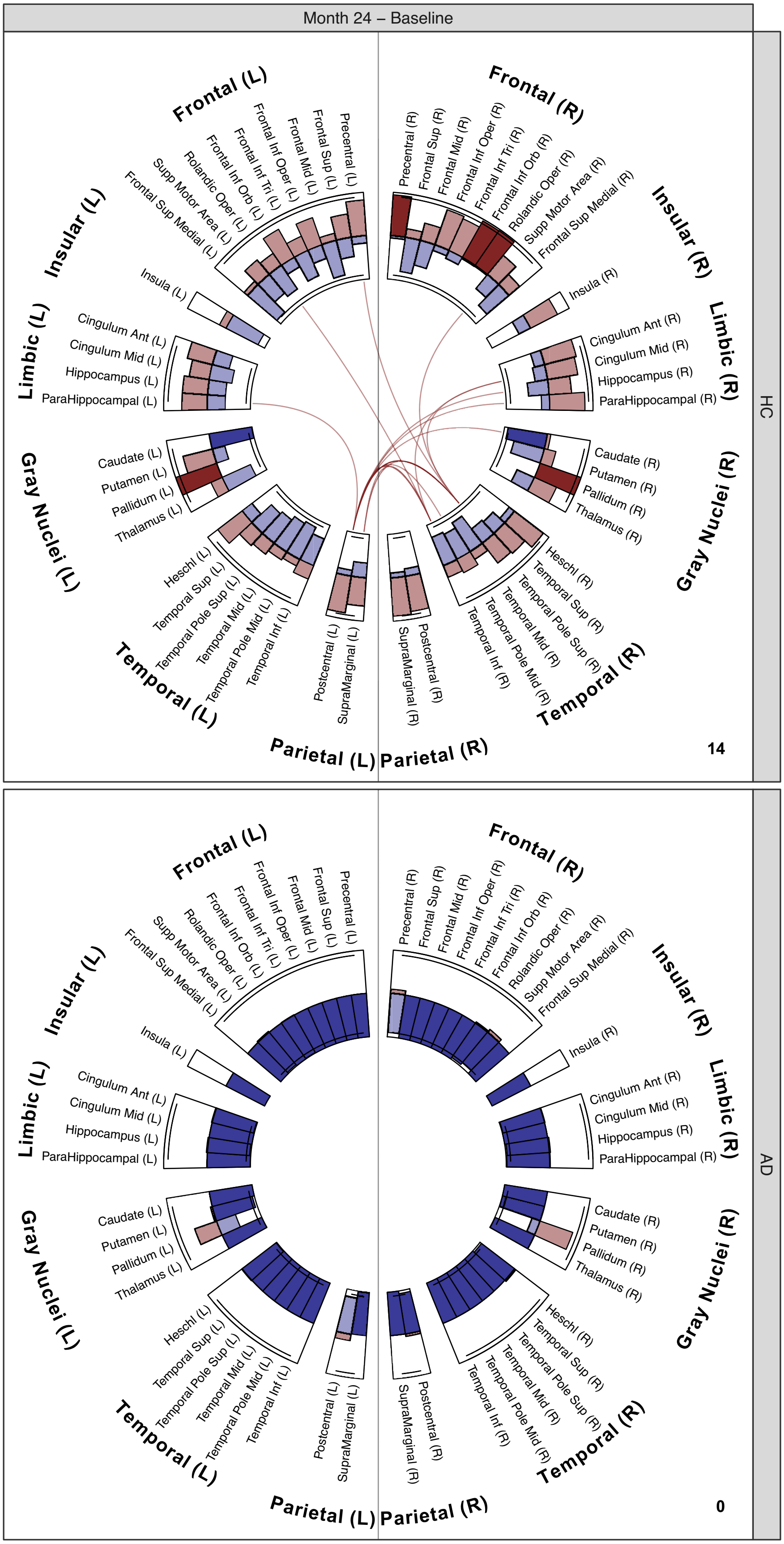

FIGURE 2 Legend on next page.

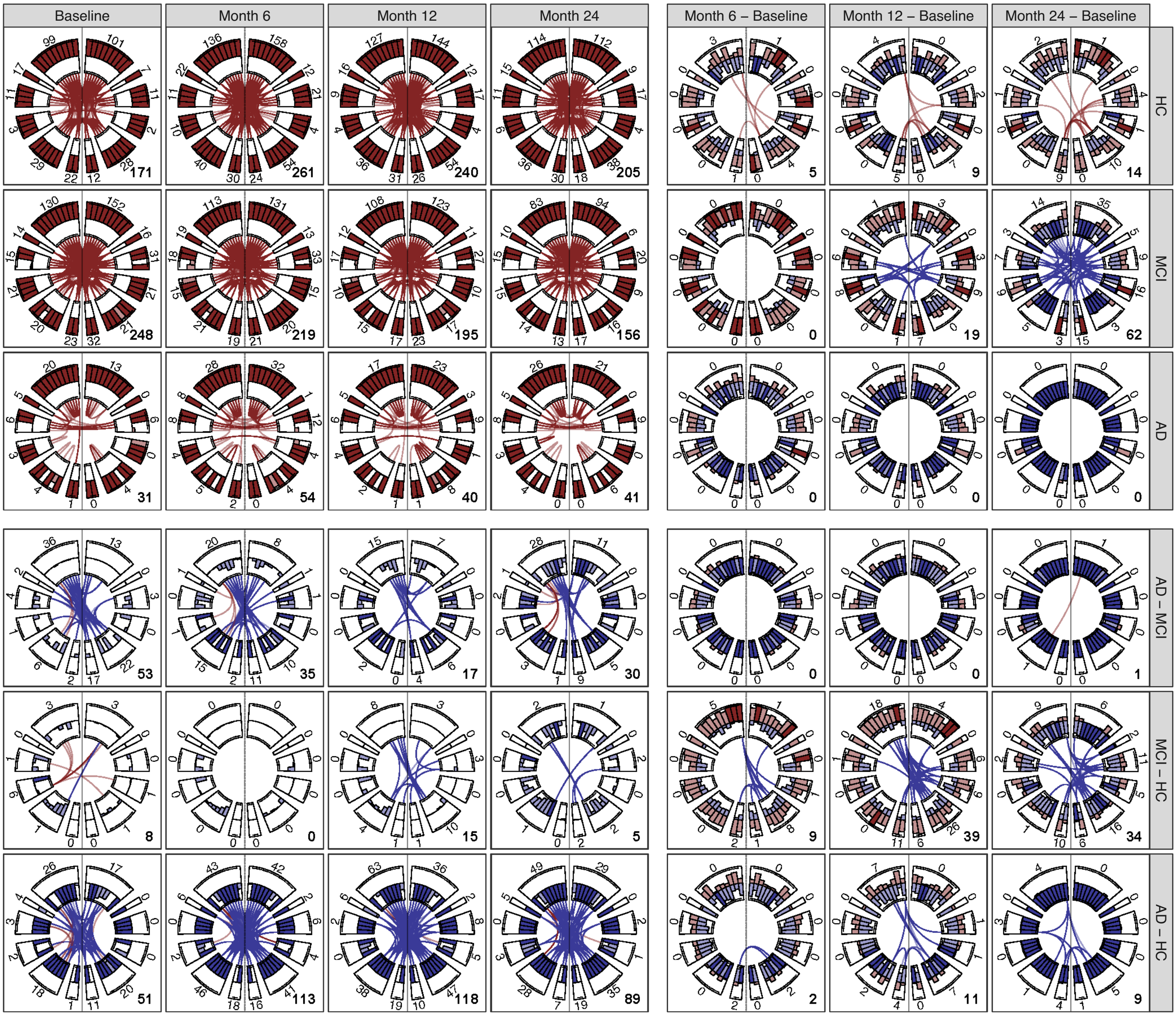

FIGURE 3 Metabolic connectivity and activity: Arcs indicate high probability of contrasted metabolic connectivity between regions ($P_\delta^+(\rho) > 0.9$ in red, or $P_\delta^-(\rho) > 0.9$ in blue). (For connectivity, the exceedance values $\delta = 0.5$ for the upper left block, $\delta = 0.1$ for the lower left group differences block, and zero for the remaining two blocks.) Rectangles along the outer segment provide both probabilities $P_\delta^+(\theta)$ (in red) and $P_\delta^-(\theta)$ (in blue), back to back, indicating the probability of contrasted metabolic activity for each region. (For activity, the exceedance values $\delta = 0.75$ for the upper left block, $\delta = 0.05$ for the lower left group differences block, and zero for the remaining two blocks.) Dark rectangles represent probabilities exceeding 90%. Each segment represents an anatomical sector of the brain, and the accompanying numbers indicate the number of arcs impinging on that sector. The number of connected region pairs is indicated in the lower right-hand corner of each panel.

In the $\langle\cdot\rangle \times \langle\cdot\rangle$ block of uncontrasted Group × Visit combinations, metabolic uptake and connectivity for all groups and visits are strongly positive. However, the increased threshold δ to 0.5 reveals a distinct difference in the connectivity of $\langle \mathrm{AD}\rangle \times \langle\cdot\rangle$ compared to $\langle \mathrm{HC}\rangle \times \langle\cdot\rangle$ and $\langle \mathrm{MCI}\rangle \times \langle\cdot\rangle$ in the block of zero-difference contrasts:

FIGURE 2 Metabolic connectivity and activity: group change over time. Arcs indicate high probability of metabolic connectivity change from baseline to Month 24: red arcs for $P_{\delta=0}^+(\rho_{\mathrm{M24}}) - \rho_{\mathrm{BL}} > 0.9$, blue arcs for $P_{\delta=0}^-(\rho_{\mathrm{M24}}) - \rho_{\mathrm{BL}} > 0.9$. The outer rings, in red and blue, probability of change in metabolic activity over time: red for high probability of positive change from baseline to Month 24; blue for negative. The number of connected region pairs is indicated in the lower right-hand corner of each panel.

TABLE 2 Region pair association of the change in uptake 24 Months − Baseline between groups. Region pairs whose probability of either positive or negative association for the double contrast that exceeds 95% are listed. Also listed are the corresponding per-group probabilities for 24 Months − Baseline change and the corresponding differences in posterior average correlation. Regions highlighted in red demonstrate significant change in activation, as listed in Table 1.

(a) ⟨AD − MCI⟩ × ⟨24 Months − Baseline⟩

		Probability			Contrast		
		AD − MCI	AD	MCI	AD − MCI	AD	MCI
Positive							
Frontal Mid (R)	Temporal Mid (L)	0.907	0.817	0.143	0.235	0.148	−0.087

(b) ⟨MCI − HC⟩ × ⟨24 Months − Baseline⟩

		Probability			Contrast		
		MCI − HC	MCI	HC	MCI − HC	MCI	HC
Negative							
Postcentral (L)	Temporal Pole Sup (R)	0.019	0.126	0.959	−0.350	−0.112	0.238
	Temporal Inf (R)	0.043	0.175	0.927	−0.270	−0.087	0.183
	Temporal Pole Mid (R)	0.092	0.335	0.906	−0.228	−0.042	0.186
Caudate (R)	Postcentral (L)	0.026	0.070	0.914	−0.344	−0.141	0.203
	Precentral (L)	0.058	0.116	0.863	−0.280	−0.114	0.167
	Postcentral (R)	0.063	0.048	0.784	−0.263	−0.151	0.112
	Supp Motor Area (R)	0.078	0.032	0.684	−0.253	−0.182	0.071
	SupraMarginal (L)	0.095	0.257	0.872	−0.227	−0.058	0.169
ParaHippocampal (R)	Postcentral (L)	0.030	0.152	0.942	−0.317	−0.097	0.220
	Postcentral (R)	0.046	0.079	0.861	−0.277	−0.132	0.146
	Supp Motor Area (R)	0.056	0.080	0.835	−0.285	−0.139	0.145
	Precentral (L)	0.078	0.278	0.905	−0.248	−0.057	0.190
Hippocampus (R)	Postcentral (L)	0.037	0.118	0.914	−0.306	−0.115	0.190
	Postcentral (R)	0.075	0.053	0.746	−0.242	−0.151	0.092
	Precentral (L)	0.084	0.173	0.848	−0.245	−0.092	0.153
Precentral (L)	Temporal Pole Sup (R)	0.045	0.182	0.922	−0.282	−0.081	0.201
	Temporal Inf (R)	0.098	0.288	0.885	−0.203	−0.051	0.152
Supp Motor Area (R)	Temporal Pole Sup (R)	0.046	0.121	0.893	−0.296	−0.116	0.181
	Temporal Inf (R)	0.071	0.071	0.776	−0.248	−0.144	0.105
	Temporal Pole Mid (R)	0.094	0.242	0.866	−0.231	−0.069	0.162
Postcentral (R)	Temporal Pole Sup (R)	0.048	0.083	0.866	−0.286	−0.126	0.160
	Temporal Pole Sup (L)	0.098	0.117	0.778	−0.219	−0.111	0.108
Rolandic Oper (L)	Temporal Inf (R)	0.059	0.240	0.925	−0.218	−0.060	0.158
	Temporal Mid (R)	0.096	0.241	0.869	−0.176	−0.056	0.120
Insula (R)	Postcentral (L)	0.062	0.037	0.762	−0.234	−0.139	0.095
	Precentral (L)	0.096	0.086	0.758	−0.197	−0.107	0.090
Precentral (R)	Temporal Pole Sup (R)	0.084	0.130	0.818	−0.233	−0.106	0.126
Cingulum Mid (R)	ParaHippocampal (R)	0.087	0.217	0.865	−0.223	−0.072	0.151
	Temporal Inf (R)	0.099	0.343	0.901	−0.209	−0.035	0.175
	Temporal Pole Sup (R)	0.100	0.385	0.911	−0.217	−0.028	0.189
SupraMarginal (L)	Temporal Pole Sup (R)	0.092	0.349	0.908	−0.209	−0.037	0.172

(Continues)

TABLE 2 (Continued)

(b) $\langle \text{MCI} - \text{HC} \rangle \times \langle \text{24 Months} - \text{Baseline} \rangle$

		Probability			**Contrast**		
		MCI − HC	**MCI**	**HC**	**MCI − HC**	**MCI**	**HC**
Supp Motor Area (L)	Temporal Pole Sup (R)	0.093	0.206	0.854	−0.230	−0.082	0.147
Hippocampus (L)	Postcentral (R)	0.095	0.083	0.748	−0.223	−0.127	0.096
ParaHippocampal (L)	Supp Motor Area (R)	0.096	0.194	0.834	−0.234	−0.091	0.143

(c) $\langle \text{AD} - \text{HC} \rangle \times \langle \text{24 Months} - \text{Baseline} \rangle$

		Probability			**Contrast**		
		AD − HC	**AD**	**HC**	**AD − HC**	**AD**	**HC**
Negative							
Postcentral (L)	Temporal Pole Sup (R)	0.040	0.196	0.959	−0.380	−0.142	0.238
	Temporal Pole Mid (R)	0.073	0.211	0.906	−0.329	−0.143	0.186
Precentral (L)	Temporal Pole Sup (R)	0.051	0.174	0.922	−0.359	−0.158	0.201
	Temporal Pole Mid (L)	0.073	0.133	0.823	−0.324	−0.201	0.123
	Temporal Pole Mid (R)	0.077	0.195	0.887	−0.320	−0.153	0.167
ParaHippocampal (L)	Postcentral (L)	0.071	0.226	0.917	−0.333	−0.136	0.197
	Precentral (L)	0.086	0.228	0.894	−0.309	−0.129	0.180
	Postcentral (R)	0.092	0.166	0.816	−0.304	−0.173	0.131
SupraMarginal (L)	Temporal Pole Sup (R)	0.091	0.245	0.908	−0.287	−0.115	0.172

both the temporal and parietal sectors, bilaterally, appear to lose strong connections with the anatomical sectors in the rest of the brain.

In the $\langle - \rangle \times \langle \cdot \rangle$ group difference contrast block, virtually all differences in uptake are highly probably negative across all visits and all group combinations. Consistent with the observations above, contrast $\langle \text{MCI-HC} \rangle \times \langle \cdot \rangle$ shows fewer connected region pairs that compared to the contrasts involving AD.

For change over time, $\langle \text{MCI} \rangle \times \langle - \rangle$ shows a growing number of region-pairs with declining correlation relative to baseline. The $\langle \text{HC} \rangle \times \langle - \rangle$ shows a slight increase in correlation relative to baseline for a small number of region-pairs. We note, as well, a progressive decline in uptake in virtually all regions for groups MCI and (especially) AD.

Finally, for the $\langle - \rangle \times \langle - \rangle$ contrast block, the connectivity difference $\langle \text{AD} - \text{MCI} \rangle \times \langle - \rangle$ does not seem to change over visits relative to baseline; however, the corresponding change in uptake ends up solidly negative by Month 24. The connection profile of the group difference $\langle \text{MCI} - \text{HC} \rangle \times \langle - \rangle$ shows a somewhat consistent set of region-pairs with decreased connectivity relative to baseline, whereas the change in uptake of the group difference seems to exhibit an increase in Month 6 and Month 12, but shows a marked decrease at Month 24.

4.2.2 | Via posterior median

Table 2 lists the pairwise connections shown in Figure 3 for contrasts $\langle - \rangle \times \langle \text{Month 24} - \text{Baseline} \rangle$. The subtables for each pair of groups provide both the change in group differences from baseline to the visit at Month 24 along with the corresponding single-contrasts indicating each individual group's change over the same interval. Values are given for the inferred probability values as well as the corresponding differences in the posterior median correlation matrix for comparison purposes.

We note that for contrast $\langle \text{AD} - \text{MCI} \rangle \times \langle \text{Month 24} \rangle - \text{Baseline}$, no region-pairs exceeded the 90% threshold. Both $\langle \text{MCI} - \text{HC} \rangle \times \langle \text{Month 24} \rangle - \text{Baseline}$ and $\langle \text{AD} - \text{HC} \rangle \times \langle \text{Month 24} \rangle - \text{Baseline}$ exhibit a similar pattern: changes in the posterior median correlation for HC are generally positive, agreeing with the inferred probability values exceeding

0.5, whereas changes in the posterior median correlation for MCI and AD are consistently negative, resulting in group differences with HC that are even more negative. These findings are reflected in the corresponding inferred probabilities which are well below 0.5.

5 | CONCLUSION

Our between-group metabolic activity results largely corroborate findings in the literature, summarized by Brown et al. (2014); Patterson et al. (2011); Shivamurthy et al. (2015), with decreased uptake in the temporal and parietal lobes in AD relative to HC. We note that many regions in the MCI group tend to show an initial *increased* metabolic activity relative to baseline. By Month 24, however, only the postcentral gyrus (bilaterally) in the parietal lobe and the right pallidus among the gray nuclei show strong increased activity. This hypermetabolism has been hypothesized to be a compensatory mechanism to counteract the general decrease in activity overall (Ashraf et al., 2014). the parietal lobe Delbeuck et al. (2003) characterize AD as a "disconnectivity" syndrome, citing evidence from neuropathology, electrophysiology and neuroimaging, and neuropsychological testing. In support of this view, our model highlights strongly reduced inter-hemispheric connections in AD, relative to HC, in the temporal, parietal, and frontal lobes; and subcortical gray nuclei. Alterations—decreases—in connectivity seem to occur primarily during the MCI phase over time; AD exhibits no significant change in connectivity over time. We are unsure what to make of the increased metabolic association relative to baseline for HC; it may be an artifact of our choice of reference region for intensity normalization (Rasmussen et al., 2012; Yakushev et al., 2008), or a reflection of age-related alterations. Also, we note decreased connectivity between the temporal, parietal, and frontal lobes in AD versus HC, similar to analyses (Alexander & Moeller, 1994; Huang et al., 2018). Several studies use longitudinal change in FDG activity relative to baseline as features for classifiers that differentiate between cognitively normal controls and MCI or AD patients (Gray et al., 2012; Rodrigues & Silveira, 2014; Shokouhi et al., 2013; Teng et al., 2020). However, to our knowledge, no study has formally quantified the evolution of group differences in metabolic activity or connectivity in a longitudinal setting.

A variety of statistical approaches have been developed to analyze PET-based measures of metabolic activity and connectivity. These approaches typically focus on either activity or connectivity, but not both in a consistent manner. In contrast, the BSMac approach jointly models univariate metabolic activity at the voxel-level and multivariate metabolic correlation at the regional level. BSMac's Bayesian formulation allows for the integration of a-priori information to be factored into the model. The voxel-based nature of the model provides the flexibility to use less common or even data-driven parcellations rather than rely on strictly anatomically-defined atlases, similar to ICA- and PCA-based approaches. BSMac also provides an alternative way to derive adjacency matrices for use in subsequent graph-theoretic analyses by acknowledging only the most probable inter-region connections. Finally, by virtue of BSMac's MCMC machinery, draws for various contrasts can be used to estimate the posterior median or mean correlation matrices, allowing for an additional means of characterizing region-pair connections.

In the current analysis, BSMac views subjects in each $\langle\text{Group}\rangle \times \langle\text{Visit}\rangle$ combination as independent; there is no consideration for longitudinal association across visits. A fully spatiotemporal model, as modeled by Bowman (2007), for example, would not be computationally feasible in this framework. However, Derado et al. (2012) augmented a variant of the BSMac model to include a multivariate conditional autoregressive component. Once trained, this augmented model was able to accurately predict activation patterns at Month 6 based on Baseline scans. In the absence of explicit temporal modeling, however, one could take the same approach used by other longitudinal studies cited here: use the difference in metabolic activity relative to the baseline visit as inputs to the model. In terms of modeling connectivity, the current implementation requires fewer regions than subjects. However, since the model characterizes connectivity through instances of the precision matrix, one could envisage embedding a SICE-like procedure to take advantage of sparse connectivity (Emmert-Streib et al., 2019). Such an extension would leverage the known sparsity of brain connections to relax the constraint on the number of regions.

AUTHOR CONTRIBUTIONS

Daniel Drake: Data curation (supporting); formal analysis (supporting); investigation (equal); software (supporting); visualization (lead); writing – original draft (lead); writing – review and editing (lead). **Gordana Derado:** Conceptualization (equal); data curation (equal); formal analysis (equal); investigation (equal); software (supporting); writing – review and editing (equal). **Lijun Zhang:** Conceptualization (equal); software (lead). **F. DuBois Bowman:** Conceptualization (lead); formal analysis (lead); funding acquisition (lead); investigation (equal); methodology (lead); project administration (lead); resources (lead); software (equal); supervision (lead); writing – review and editing (equal).

ACKNOWLEDGMENTS

Data collection and sharing for this project was funded by the Alzheimer's Disease Neuroimaging Initiative (ADNI) (National Institutes of Health Grant U01 AG024904) and DOD ADNI (Department of Defense award number W81XWH-12-2-0012). ADNI is funded by the National Institute on Aging, the National Institute of Biomedical Imaging and Bioengineering, and through generous contributions from the following: AbbVie, Alzheimer's Association; Alzheimer's Drug Discovery Foundation; Araclon Biotech; BioClinica, Inc.; Biogen; Bristol-Myers Squibb Company; CereSpir, Inc.; Cogstate; Eisai Inc.; Elan Pharmaceuticals, Inc.; Eli Lilly and Company; EuroImmun; F. Hoffmann-La Roche Ltd and its affiliated company Genentech, Inc.; Fujirebio; GE Healthcare; IXICO Ltd.; Janssen Alzheimer Immunotherapy Research & Development, LLC.; Johnson & Johnson Pharmaceutical Research & Development LLC.; Lumosity; Lundbeck; Merck & Co., Inc.; Meso Scale Diagnostics, LLC.; NeuroRx Research; Neurotrack Technologies; Novartis Pharmaceuticals Corporation; Pfizer Inc.; Piramal Imaging; Servier; Takeda Pharmaceutical Company; and Transition Therapeutics. The Canadian Institutes of Health Research is providing funds to support ADNI clinical sites in Canada. Private sector contributions are facilitated by the Foundation for the National Institutes of Health (www.fnih.org). The grantee organization is the Northern California Institute for Research and Education, and the study is coordinated by the Alzheimer's Therapeutic Research Institute at the University of Southern California. ADNI data are disseminated by the Laboratory for Neuro Imaging at the University of Southern California. The authors would also like to thank Dr. Jonathan Nye at Emory University for helpful discussions regarding reference region scaling.

FUNDING INFORMATION

The work of Drake and Bowman was supported by the NINDS Morris K. Udall Centers of Excellence for Parkinson's Disease Research Grant P50NS123067.

DATA AVAILABILITY STATEMENT

The data that support the findings of this study are available from the Alzheimer's Disease Neuroimaging Initiative (ADNI). Restrictions apply to the availability of these data, which were used under license for this study. Data are available at https://adni.loni.usc.edu with the permission of the LONI Image and Data Archive.

ORCID

Daniel F. Drake https://orcid.org/0000-0003-3308-8873
Gordana Derado https://orcid.org/0000-0002-3346-0770
Lijun Zhang https://orcid.org/0000-0003-4974-2745
F. DuBois Bowman https://orcid.org/0000-0002-3204-6535

RELATED WIREs ARTICLES

Some recent statistical learning methods for longitudinal high-dimensional data

REFERENCES

Alexander, G. E., & Moeller, J. R. (1994). Application of the scaled subprofile model to functional imaging in neuropsychiatric disorders: A principal component approach to modeling brain function in disease. *Human Brain Mapping*, *2*(1–2), 79–94.

Ashraf, A., Fan, Z., Brooks, D. J., & Edison, P. (2014). Cortical hypermetabolism in MCI subjects: A compensatory mechanism? *European Journal of Nuclear Medicine and Molecular Imaging*, *42*(3), 447–458.

Bani Asadi, N., Rish, I., Scheinberg, K., Kanevsky, D., & Ramabhadran, B. (2009). Map approach to learning sparse Gaussian Markov networks. In *2009 IEEE international conference on acoustics, speech and signal processing* (pp. 1721–1724). IEEE.

Bowman, F. D. (2005). Spatio-temporal modeling of localized brain activity. *Biostatistics*, *6*, 558–575.

Bowman, F. D. (2007). Spatiotemporal models for region of interest analyses of functional neuroimaging data. *Journal of the American Statistical Association*, *102*(478), 442–453.

Bowman, F. D., Caffo, B., Bassett, S. S., & Kilts, C. (2008). A Bayesian hierarchical framework for spatial modeling of fMRI data. *NeuroImage*, *39*(1), 146–156.

Brown, R. K. J., Bohnen, N. I., Wong, K. K., Minoshima, S., & Frey, K. A. (2014). Brain PET in suspected dementia: Patterns of altered FDG metabolism. *Radiographics*, *34*(3), 684–701 PMID: 24819789.

Bullmore, E., & Sporns, O. (2009). Complex brain networks: Graph theoretical analysis of structural and functional systems. *Nature Reviews Neuroscience*, *10*(3), 186–198.

Calhoun, V. D., Adali, T., Giuliani, N. R., Pekar, J. J., Kiehl, K. A., & Pearlson, G. D. (2006). Method for multimodal analysis of independent source differences in schizophrenia: Combining gray matter structural and auditory oddball functional data. *Human Brain Mapping*, *27*, 47–62.

Calhoun, V. D., Adali, T., Kiehl, K. A., Astur, R., Pekar, J. J., & Pearlson, G. D. (2006). A method for multitask fMRI data fusion applied to schizophrenia. *Human Brain Mapping*, *27*, 598–610.

Carbonell, F., Charil, A., Zijdenbos, A. P., Evans, A. C., Bedell, B. J., & for the Alzheimer's Disease Neuroimaging Initiative. (2014). Hierarchical multivariate covariance analysis of metabolic connectivity. *Journal of Cerebral Blood Flow & Metabolism*, *34*(12), 1936–1943.

Chung, J., Yoo, K., Kim, E., Na, D. L., & Jeong, Y. (2016). Glucose metabolic brain networks in early-onset vs. late-onset Alzheimer's disease. *Frontiers in Aging Neuroscience*, *8*, 159.

Delbeuck, X., Van der Linden, M., & Collette, F. (2003). Alzheimer's disease as a disconnection syndrome? *Neuropsychology Review*, *13*, 79–92.

Dempster, A. P. (1972). Covariance selection. *Biometrics*, *28*(1), 157.

Derado, G., Bowman, F. D., Zhang, L., & Alzheimer's Disease Neuroimaging Initiative Investigators. (2013). Predicting brain activity using a Bayesian spatial model. *Statistical Methods in Medical Research*, *22*, 382–397.

Derado, G., Bowman, F. D., Zhang, L., & the Alzheimer's Disease Neuroimaging Initiative. (2012). Predicting brain activity using a Bayesian spatial model. *Statistical Methods in Medical Research*, *22*(4), 382–397.

Eidelberg, D. (2009). Metabolic brain networks in neurodegenerative disorders: A functional imaging approach. *Trends in Neurosciences*, *32*(10), 548–557.

Eklund, A., Nichols, T. E., & Knutsson, H. (2016). Cluster failure: Why fMRI inferences for spatial extent have inflated false-positive rates. *Proceedings of the National Academy of Sciences*, *113*(28), 7900–7905.

Emmert-Streib, F., Tripathi, S., & Dehmer, M. (2019). Constrained covariance matrices with a biologically realistic structure: Comparison of methods for generating high-dimensional gaussian graphical models. *Frontiers in Applied Mathematics and Statistics*, *5*, Article 37.

Fletcher, P. T., Venkatasubramanian, S., & Joshi, S. (2008). Robust statistics on Riemannian manifolds via the geometric median. In *2008 IEEE Conference on Computer Vision and Pattern Recognition*. IEEE.

Friedman, J., Hastie, T., & Tibshirani, R. (2007). Sparse inverse covariance estimation with the graphical lasso. *Translational Neuroscience*, *9*(3), 432–441.

Friston, K. J., Frith, C. D., Liddle, P. F., & Frackowiak, R. S. (1991). Comparing functional (PET) images: The assessment of significant change. *Journal of Cerebral Blood Flow and Metabolism*, *11*, 690–699.

Friston, K. J., Holmes, A. P., Worsley, K. J., Poline, J.-P., Frith, C. D., & Frackowiak, R. S. J. (1995). Statistical parametric maps in functional imaging: A general linear approach. *Human Brain Mapping*, *2*(4), 189–210.

Ganz, M., Nørgaard, M., Beliveau, V., Svarer, C., Knudsen, G. M., & Greve, D. N. (2020). False positive rates in positron emission tomography (PET) voxelwise analyses. *Journal of Cerebral Blood Flow & Metabolism*, *41*(7), 1647–1657.

Gray, K. R., Wolz, R., Heckemann, R. A., Aljabar, P., Hammers, A., & Rueckert, D. (2012). Multi-region analysis of longitudinal FDG-PET for the classification of alzheimer's disease. *NeuroImage*, *60*(1), 221–229.

Groves, A. R., Beckmann, C. F., Smith, S. M., & Woolrich, M. W. (2011). Linked independent component analysis for multimodal data fusion. *NeuroImage*, *54*(3), 2198–2217.

Horwitz, B., Duara, R., & Rapoport, S. I. (1984). Intercorrelations of glucose metabolic rates between brain regions: Application to healthy males in a state of reduced sensory input. *Journal of Cerebral Blood Flow & Metabolism*, *4*(4), 484–499.

Horwitz, B., Grady, C., Schlageter, N., Duara, R., & Rapoport, S. (1987). Intercorrelations of regional cerebral glucose metabolic rates in Alzheimer's disease. *Brain Research*, *407*(2), 294–306.

Huang, S., Li, J., Sun, L., Ye, J., Fleisher, A., Wu, T., Chen, K., & Reiman, E. (2010). Learning brain connectivity of Alzheimer's disease by sparse inverse covariance estimation. *NeuroImage*, *50*(3), 935–949.

Huang, S.-Y., Hsu, J.-L., Lin, K.-J., & Hsiao, I.-T. (2020). A novel individual metabolic brain network for 18F-FDG pet imaging. *Frontiers in Neuroscience*, *14*, Article 344.

Huang, S.-Y., the Alzheimer's Disease Neuroimaging Initiative, F, Hsu, J.-L., Lin, K.-J., Liu, H.-L., Wey, S.-P., & Hsiao, I.-T. (2018). Characteristic patterns of inter- and intra-hemispheric metabolic connectivity in patients with stable and progressive mild cognitive impairment and Alzheimer's disease. *Scientific Reports*, *8*(1), 13807.

Jolliffe, I. T., & Cadima, J. (2016). Principal component analysis: A review and recent developments. *Philosophical Transactions of the Royal Society A: Mathematical, Physical and Engineering Sciences*, *374*(2065), 20150202.

Judaš, M., Cepanec, M., & Sedmak, G. (2012). Brodmann's map of the human cerebral cortex—or Brodmann's maps. *Translational Neuroscience*, *3*(1), 67–74.

Laforce, R., Tosun, D., Ghosh, P., Lehmann, M., Madison, C. M., Weiner, M. W., Miller, B. L., Jagust, W. J., & Rabinovici, G. D. (2014). Parallel ICA of FDG-PET and PiB-PET in three conditions with underlying alzheimer's pathology. *Neuroimage: Clinical*, *4*, 508–516.

Lee, D. S., Kang, H., Kim, H., Park, H., Oh, J. S., Lee, J. S., & Lee, M. C. (2008). Metabolic connectivity by interregional correlation analysis using statistical parametric mapping (SPM) and FDG brain PET; methodological development and patterns of metabolic connectivity in adults. *European Journal of Nuclear Medicine and Molecular Imaging*, *35*(9), 1681–1691.

Li, S., Jamadar, S. D., Ward, P. G. D., Egan, G. F., & Chen, Z. (2021). Estimation of simultaneous bold and dynamic FDG metabolic brain activations using a multimodality concatenated ICA (mcICA) method. *NeuroImage*, *226*, 117603.

Liu, J., Pearlson, G., Windemuth, A., Ruano, G., Perrone-Bizzozero, N. I., & Calhoun, V. (2009). Combining fMRI and SNP data to investigate connections between brain function and genetics using parallel ICA. *Human Brain Mapping*, *30*, 241–255.

Marcus, C., Mena, E., & Subramaniam, R. M. (2014). Brain PET in the diagnosis of Alzheimer's disease. *Clinical Nuclear Medicine*, *39*(10), e413–e426.

Mazziotta, J. C., Toga, A. W., Evans, A., Fox, P., & Lancaster, J. (1995). A probabilistic atlas of the human brain: Theory and rationale for its development. The International Consortium for Brain Mapping (ICBM). *NeuroImage*, *2*, 89–101.

Metter, E. J., Riege, W. H., Kameyama, M., Kuhl, D. E., & Phelps, M. E. (1984). Cerebral metabolic relationships for selected brain regions in Alzheimer's, Huntington's, and Parkinson's diseases. *Journal of Cerebral Blood Flow & Metabolism*, *4*(4), 500–506.

Metter, E. J., Riege, W. H., Kuhl, D. E., & Phelps, M. E. (1984). Cerebral metabolic relationships for selected brain regions in healthy adults. *Journal of Cerebral Blood Flow & Metabolism*, *4*(1), 1–7.

Moeller, J. R., Strother, S. C., Sidtis, J. J., & Rottenberg, D. A. (1987). Scaled subprofile model: A statistical approach to the analysis of functional patterns in positron emission tomographic data. *Journal of Cerebral Blood Flow & Metabolism*, *7*(5), 649–658.

Morbelli, S., Arnaldi, D., Capitanio, S., Picco, A., Buschiazzo, A., & Nobili, F. (2013). Resting metabolic connectivity in Alzheimer's disease. *Clinical and Translational Imaging*, *1*(4), 271–278.

Pagani, M., Öberg, J., De Carli, F., Calvo, A., Moglia, C., Canosa, A., Nobili, F., Morbelli, S., Fania, P., Cistaro, A., & Chiò, A. (2016). Metabolic spatial connectivity in amyotrophic lateral sclerosis as revealed by independent component analysis. *Human Brain Mapping*, *37*, 942–953.

Pagani, M., Salmaso, D., Rodriguez, G., Nardo, D., & Nobili, F. (2009). Principal component analysis in mild and moderate Alzheimer's disease—A novel approach to clinical diagnosis. *Psychiatry Research: Neuroimaging*, *173*(1), 8–14.

Patterson, J. C., Lilien, D. L., Takalkar, A., & Pinkston, J. B. (2011). Early detection of brain pathology suggestive of early AD using objective evaluation of FDG-PET scans. *International Journal of Alzheimer's Disease*, *2011*, 1–9.

Rahmani, F., Moghaddam, H. S., Rahmani, M., & Aarabi, M. H. (2020). Metabolic connectivity in Alzheimer's diseases. *Clinical and Translational Imaging*, *8*(3), 157–166.

Rasmussen, J. M., Lakatos, A., van Erp, T. G., Kruggel, F., Keator, D. B., Fallon, J. T., Macciardi, F., & Potkin, S. G. (2012). Empirical derivation of the reference region for computing diagnostic sensitive ^{18}fluorodeoxyglucose ratios in Alzheimer's disease based on the ADNI sample. *Biochimica et Biophysica Acta (BBA)—Molecular Basis of Disease*, *1822*(3), 457–466.

Rodrigues, F., & Silveira, M. (2014). Longitudinal FDG-PET features for the classification of Alzheimer's disease. In *2014 36th Annual International Conference of the IEEE Engineering in Medicine and Biology Society*. IEEE.

Scarmeas, N., Habeck, C. G., Zarahn, E., Anderson, K. E., Park, A., Hilton, J., Pelton, G. H., Tabert, M. H., Honig, L. S., Moeller, J. R., Devanand, D. P., & Stern, Y. (2004). Covariance pet patterns in early Alzheimer's disease and subjects with cognitive impairment but no dementia: Utility in group discrimination and correlations with functional performance. *NeuroImage*, *23*(1), 35–45.

Shivamurthy, V. K. N., Tahari, A. K., Marcus, C., & Subramaniam, R. M. (2015). Brain FDG PET and the diagnosis of dementia. *American Journal of Roentgenology*, *204*(1), W76–W85.

Shokouhi, S., Claassen, D., Kang, H., Ding, Z., Rogers, B., Mishra, A., Riddle, W. R., & The Alzheimer's Disease Neuroimaging Initiative. (2013). Longitudinal progression of cognitive decline correlates with changes in the spatial pattern of brain 18F-FDG PET. *Journal of Nuclear Medicine*, *54*, 1564–1569.

Spetsieris, P. G., & Eidelberg, D. (2021). Spectral guided sparse inverse covariance estimation of metabolic networks in Parkinson's disease. *NeuroImage*, *226*, 117568.

Stone, J. V. (2002). Independent component analysis: An introduction. *Trends in Cognitive Sciences*, *6*(2), 59–64.

Teng, L., Li, Y., Zhao, Y., Hu, T., Zhang, Z., Yao, Z., Hu, B., & for the Alzheimer's Disease Neuroimaging Initiative. (2020). Predicting MCI progression with FDG-PET and cognitive scores: A longitudinal study. *BMC Neurology*, *20*, 148.

Titov, D., Diehl-Schmid, J., Shi, K., Perneczky, R., Zou, N., Grimmer, T., Li, J., Drzezga, A., & Yakushev, I. (2016). Metabolic connectivity for differential diagnosis of dementing disorders. *Journal of Cerebral Blood Flow & Metabolism*, *37*(1), 252–262.

Toussaint, P.-J., Perlbarg, V., Bellec, P., Desarnaud, S., Lacomblez, L., Doyon, J., Habert, M.-O., & Benali, H. (2012). Resting state FDG-PET functional connectivity as an early biomarker of Alzheimer's disease using conjoint univariate and independent component analyses. *NeuroImage*, *63*(2), 936–946.

Tzourio-Mazoyer, N., Landeau, B., Papathanassiou, D., Crivello, F., Etard, O., Delcroix, N., Mazoyer, B., & Joliot, M. (2002). Automated anatomical labeling of activations in SPM using a macroscopic anatomical parcellation of the MNI MRI single-subject brain. *NeuroImage*, *15*, 273–289.

Veronese, M., Moro, L., Arcolin, M., Dipasquale, O., Rizzo, G., Expert, P., Khan, W., Fisher, P. M., Svarer, C., Bertoldo, A., Howes, O., & Turkheimer, F. E. (2019). Covariance statistics and network analysis of brain pet imaging studies. *Scientific Reports*, *9*(1), 2496.

Wang, M., Jiang, J., Yan, Z., Alberts, I., Ge, J., Zhang, H., Zuo, C., Yu, J., Rominger, A., Shi, K., & the Alzheimer's Disease Neuroimaging Initiative. (2020). Individual brain metabolic connectome indicator based on Kullback–Leibler divergence similarity estimation predicts progression from mild cognitive impairment to Alzheimer's dementia. *European Journal of Nuclear Medicine and Molecular Imaging*, *47*, 2753–2764.

Wang, M., Yan, Z., Xiao, S. Y., Zuo, C., & Jiang, J. (2020). A novel metabolic connectome method to predict progression to mild cognitive impairment. *Behavioural Neurology*, *2020*, 2825037.

Yakushev, I., Drzezga, A., & Habeck, C. (2017). Metabolic connectivity: Methods and applications. *Current Opinion in Neurology*, *30*(6), 677–685.

Yakushev, I., Landvogt, C., Buchholz, H.-G., Fellgiebel, A., Hammers, A., Scheurich, A., Schmidtmann, I., Gerhard, A., Schreckenberger, M., & Bartenstein, P. (2008). Choice of reference area in studies of alzheimer's disease using positron emission tomography with fluorodeoxyglucose-F18. *Psychiatry Research: Neuroimaging*, *164*(2), 143–153.

Yang, W., Pilozzi, A., & Huang, X. (2021). An overview of ICA/BSS-based application to Alzheimer's brain signal processing. *Biomedicine*, *9*(4), 386.

Zhang, L., Agravat, S., Derado, G., Chen, S., McIntosh, B., & Bowman, F. (2012). BSMac: A MATLAB toolbox of Bayesian spatial model for brain activation and connectivity. *Journal of Neuroscience Methods*, *204*, 133–143.

How to cite this article: Drake, D. F., Derado, G., Zhang, L., Bowman, F. D., & for the Alzheimer's Disease Neuroimaging Initiative (2023). Neuroimaging statistical approaches for determining neural correlates of Alzheimer's disease via positron emission tomography imaging. *WIREs Computational Statistics*, *15*(5), e1606. https://doi.org/10.1002/wics.1606